

A primary noise thermometer for ultracold Bose gases

This content has been downloaded from IOPscience. Please scroll down to see the full text.

2006 New J. Phys. 8 189

(<http://iopscience.iop.org/1367-2630/8/9/189>)

View [the table of contents for this issue](#), or go to the [journal homepage](#) for more

Download details:

IP Address: 147.142.186.54

This content was downloaded on 18/09/2015 at 10:27

Please note that [terms and conditions apply](#).

A primary noise thermometer for ultracold Bose gases

R Gati¹, J Esteve, B Hemmerling, T B Ottenstein, J Appmeier, A Weller and M K Oberthaler

Kirchhoff-Institut für Physik, Universität Heidelberg,
Im Neuenheimer Feld 227, 69120 Heidelberg, Germany
E-mail: [noisethermometry@matterwave.de](mailto:noise thermometer@matterwave.de)

New Journal of Physics **8** (2006) 189

Received 9 June 2006

Published 12 September 2006

Online at <http://www.njp.org/>

doi:10.1088/1367-2630/8/9/189

Abstract. We discuss in detail the experimental investigation of thermally induced fluctuations of the relative phase between two weakly coupled Bose–Einstein condensates (BECs). In analogy to superconducting Josephson junctions, the weak coupling originates from a tunnelling process through a potential barrier which is obtained by trapping the condensates in an optical double-well potential. The observed fluctuations of the relative phase are in quantitative agreement with a many body two mode model at finite temperature. The agreement demonstrates the possibility of using the phase fluctuation measurements in a bosonic Josephson junction (BJJ) as a primary thermometer. This new method allows for measuring temperatures far below the critical temperature where standard methods based on time of flight measurements fail. We employ this new thermometer to probe the heat capacity of a degenerate Bose gas as a function of temperature.

¹ Author to whom any correspondence should be addressed.

Contents

1. Introduction	2
2. Phase fluctuations within the two mode approximation	3
2.1. The two mode approximation	3
2.2. Calculation of the coherence factor	6
2.3. Finite temperature	7
3. Experimental protocol	9
4. Coherence factor—scaling law for phase fluctuations	12
5. Thermalization	14
6. Application of the thermometer to heat capacity measurement	15
7. Conclusion	17
Acknowledgments	17
References	17

1. Introduction

Among other methods [1, 2], a stable double-well potential for Bose–Einstein condensates (BECs) can be realized by superimposing a three-dimensional (3D) harmonic trapping potential and a 1D optical lattice with large periodicity [3]. If the height of the potential barrier in the centre of the trap becomes comparable to the chemical potential, the BEC is split into two parts. If the barrier height is not too high, the two split condensates are still weakly coupled via tunnelling through the barrier in analogy to superconducting Josephson junctions [4, 5] and superfluid Helium weak links [6].

At equilibrium, the relative phase between the two coupled condensates fluctuates because of quantum fluctuations [7]–[9] and thermally induced fluctuations [10]. The experiments discussed in this paper are performed in the so-called ‘classical Josephson regime’ where quantum mechanical fluctuations are negligible and thermally induced fluctuations can be treated classically. As shown in [10], the phase fluctuations in this regime depend only on a single parameter given by the ratio of the thermal energy and the tunnelling coupling strength between the two wells.

The dependence of the phase fluctuations on temperature allows for the application of the fluctuation measurements for thermometry [11]. Hereby the coherence factor, or to be more precise the distribution of the relative phases, is measured experimentally and compared to the theoretical prediction. Standard methods to estimate temperature in Bose–Einstein condensed atomic samples usually rely on time of flight measurements. The temperature is deduced after ballistic expansion either from the expansion velocity of the thermal cloud or from the ratio of the condensed to the non condensed populations. This method starts to fail for temperatures far below the critical temperature where the number of particles in the thermal cloud becomes small compared to the number of particles in the BEC. However, even in this regime, the phase fluctuation method can be applied as the coupling strength can be tuned via the barrier height in order to make the bosonic Josephson junction (BJJ) sensitive to thermally induced effects.

Experimentally the relative phase between the BECs can be accessed by time of flight during which the two condensates expand and interfere [12]. The resulting density profile is analogous

to the intensity profile observed with coherent light in double-slit interference experiments and the relative phase can be deduced from the position of the interference peaks with respect to their envelope. Interference patterns are observable for any temperature as far as the BEC fraction is large enough for detection. Hereby the visibility of the patterns increases with decreasing temperature making the investigation of the thermally induced fluctuations accessible for a wide range of temperatures.

Thermally induced phase fluctuations have been observed so far in elongated BECs [13, 14]. In these quasi 1D BEC, the coherence of the whole cloud is diminished by the thermally populated low lying excitations. In time of flight, these excitations are revealed as density fringes on the BEC envelope. For low temperatures the contrast of the fringes decreases and vanishes when the typical length of the phase fluctuations becomes larger than the longitudinal extent of the condensate. The situation in the presented double-well potential is different. Here, only the coherence between the two wells is affected by thermal processes and not the coherence within each well. The fluctuations decrease and vanish for very low temperatures but increases for raising the barrier height.

In this paper, we would like to discuss the experiments presented in [11] in more detail and focus on the application of the measurements for thermometry. We justify the classical model introduced before to describe the fluctuations of the relative phase by comparing it with the prediction of a many body two mode approach. By using a more advanced calibration methods, we improved the determination of the tunnelling coupling leading to a more quantitative agreement of the experimental findings with the theoretical prediction. This allows us for the application of the phase fluctuation measurements for primary thermometry, i.e. the thermometer is calibrated directly by the theoretical model and thus the calibration with temperature measurements using other methods is not necessary.

2. Phase fluctuations within the two mode approximation

In order to use the phase fluctuation measurement as a tool for thermometry, a precise theoretical model is needed to convert the measured fluctuations into a temperature. In this section, we present in detail the two mode model that we use for this purpose. In this model, the condensate particles can occupy only two single particle states while being in thermal equilibrium with a bath composed of the non condensed atoms. We will first shortly introduce the two mode model which has attracted tremendous interest in the literature (see references 2–20 in [15]). We will then show that, because of its relative simplicity, this model allows exact numerical calculations of the phase fluctuations (or any other quantity) at finite temperature. The drastic reduction of the Hilbert space dimension due to the two mode approximation makes the two mode model one of the few exactly solvable many body systems (see for example [16]–[18]). We will compare our numerical results with analytical results that can be obtained in the low temperature and the high temperature limit.

2.1. The two mode approximation

Starting from the general many body problem of a gas of interacting bosons, the two mode approximation consists of restricting the available single particle states to two states $|\phi_1\rangle$ and $|\phi_2\rangle$. Fixing the total atom number in the sample to a given value N , a basis of the system can

then be obtained by considering the following set of Fock states

$$|n\rangle = |N - n : \phi_1, n : \phi_2\rangle \quad \text{where } n = 0, 1, \dots, N. \quad (1)$$

The dimension of the Hilbert space is then reduced to $N + 1$. This drastic reduction of the dimension allows exact numerical quantum calculations for the atom number range accessed in our experiments ($N < 10^4$).

The double-well trap used in our experiment naturally provides a geometry where the two mode approximation can be applied. Indeed, a Bogoliubov calculation of the excitation spectrum or a calculation of the Gross–Pitaevskii eigenenergies shows that the first excitation lies close to the ground state, while the second excitation is well above. As in the non interacting case, such a situation occurs only if the barrier separating the two condensates is sufficiently high (higher than the chemical potential in each well). Supposing this condition to be fulfilled, we choose for the two single particle states $|\phi_1\rangle$ and $|\phi_2\rangle$, the first two eigenstates of the Gross–Pitaevskii equation $|\phi_s\rangle$ and $|\phi_a\rangle$: $|\phi_s\rangle$ being the symmetric ground state and $|\phi_a\rangle$ the antisymmetric first excited state.² The corresponding eigenvalues are given by

$$\mu_{s,a} = \int \phi_{s,a}^* \left(-\frac{\hbar^2}{2m} \nabla^2 + V + gN|\phi_{s,a}|^2 \right) \phi_{s,a} \, d\mathbf{r}. \quad (2)$$

where g is the effective interaction strength in 3D.

Introducing the creation operators \hat{c}_s^\dagger and \hat{c}_a^\dagger associated with the two wavefunctions ϕ_s and ϕ_a , the field operator writes in the two mode approximation

$$\hat{\Psi} = \hat{c}_s \phi_s + \hat{c}_a \phi_a. \quad (3)$$

Starting from the many body Hamiltonian

$$\hat{H} = \int \left(\hat{\Psi}^\dagger \left(-\frac{\hbar^2}{2m} \nabla^2 + V \right) \hat{\Psi} + \frac{g}{2} \hat{\Psi}^\dagger \hat{\Psi}^\dagger \hat{\Psi} \hat{\Psi} \right) d\mathbf{r}, \quad (4)$$

and ignoring constant terms (terms proportional to the total atom number), we obtain the following two mode Hamiltonian [15, 19]

$$\hat{H}_{2M} = -\frac{E_J}{N} (\hat{c}_s^\dagger \hat{c}_s - \hat{c}_a^\dagger \hat{c}_a) + \frac{E_C}{8} (\hat{c}_s^\dagger \hat{c}_a + \hat{c}_a^\dagger \hat{c}_s)^2 + \frac{\delta E_C}{4} (\hat{c}_s^\dagger \hat{c}_s - \hat{c}_a^\dagger \hat{c}_a)^2 \quad (5)$$

$$= -\frac{E_J}{N} (\hat{c}_l^\dagger \hat{c}_r + \hat{c}_r^\dagger \hat{c}_l) + \frac{E_C}{8} (\hat{c}_r^\dagger \hat{c}_r - \hat{c}_l^\dagger \hat{c}_l)^2 + \frac{\delta E_C}{4} (\hat{c}_l^\dagger \hat{c}_r + \hat{c}_r^\dagger \hat{c}_l)^2. \quad (6)$$

The last equality expresses the Hamiltonian in terms of creation and annihilation operators in the left/right basis which we define as $\hat{c}_l^\dagger = (\hat{c}_s^\dagger + \hat{c}_a^\dagger)/\sqrt{2}$ and $\hat{c}_r^\dagger = (\hat{c}_s^\dagger - \hat{c}_a^\dagger)/\sqrt{2}$. The Josephson energy E_J , the charging energy E_C and the correction term δE_C are defined as follows

$$\kappa_{i,j} = \frac{g}{2} \int |\phi_i|^2 |\phi_j|^2 \, d\mathbf{r} \quad (\text{with } i, j = s, a), \quad (7)$$

² We assume the wavefunctions ϕ_s and ϕ_a to be normalized to one.

$$E_C = 8\kappa_{s,a}, \quad (8)$$

$$E_J = \frac{N}{2}(\mu_a - \mu_s) - \frac{N(N+1)}{2}(\kappa_{a,a} - \kappa_{s,s}), \quad (9)$$

$$\delta E_C = \frac{\kappa_{s,s} + \kappa_{a,a} - 2\kappa_{s,a}}{4}. \quad (10)$$

The first term of the two mode Hamiltonian which is proportional to E_J describes the tunnelling between the two wells. It is diagonal in the symmetric–antisymmetric basis. The second term proportional to E_C describes the on-site interaction in each well and is diagonal in the left–right basis. The last term is a correction term that, as we will see, can usually be neglected.

In the high barrier limit, the different interaction coefficients $\kappa_{i,j}$ can be considered to be equal and the correction term δE_C vanishes. In our experimental parameter range, we find this term to be less than $10^{-5} \cdot E_J/N$ and less than $10^{-3} \cdot E_C/8$. The correction term is included in our numerical calculations, however its effect is so small that we will neglect it in the following discussion. To obtain the values of these three coefficients, we numerically solve the 3D Gross–Pitaevskii equation in our potential using a standard split-step iteration algorithm and propagation in imaginary time. The precision of the calculated values directly relies on the numerical precision of the employed method. In particular, the Josephson energy requires special care, because it critically depends on the difference of two energies μ_s and μ_a which are almost degenerate.

2.1.1. Eigenenergy spectrum. As mentioned above, the limited size of the Hilbert space allows exact numerical diagonalization of the two mode Hamiltonian. Our experimental parameter range is such that we always lie in the Josephson regime where the two conditions $E_C \ll E_J$ and $E_C \gg E_J/N^2$ are fulfilled. In this regime, a typical energy spectrum of the many body system looks like the one shown in figure 1(a). At low energy ($E < 2E_J$), the spectrum is almost linear and the level spacing is approximately given by the plasma frequency (see figure 1(b))

$$\omega_p = \frac{1}{\hbar} \sqrt{E_J \left(E_C + \frac{4E_J}{N^2} \right)}. \quad (11)$$

The corresponding eigenstates are delocalized over the two wells (see figure 1(c)). In a classical picture, the two mode Hamiltonian is equivalent to the Hamiltonian of a pendulum, with the relative phase corresponding to the tilt angle and the population imbalance to the momentum. In this picture, these states correspond to an oscillatory motion of the pendulum around its equilibrium (see figure 1(d)). At higher energy ($E > 2E_J$), the eigenenergies are grouped two by two. Each doublet of almost degenerate eigenstates consists of a symmetric and an antisymmetric cat-state (see figure 1(c)), however, any asymmetry between the two wells will localize the modes on the left or on the right. In the classical picture, these states correspond to a twirling motion of the pendulum. Here, the pendulum has enough energy to reach the top position and continues rotating in one direction. The degeneracy corresponds to the two possible directions of rotation. The energy of these states is dominated by the charging energy term and thus increases quadratically with the eigenstate label as expected for a free particle motion.

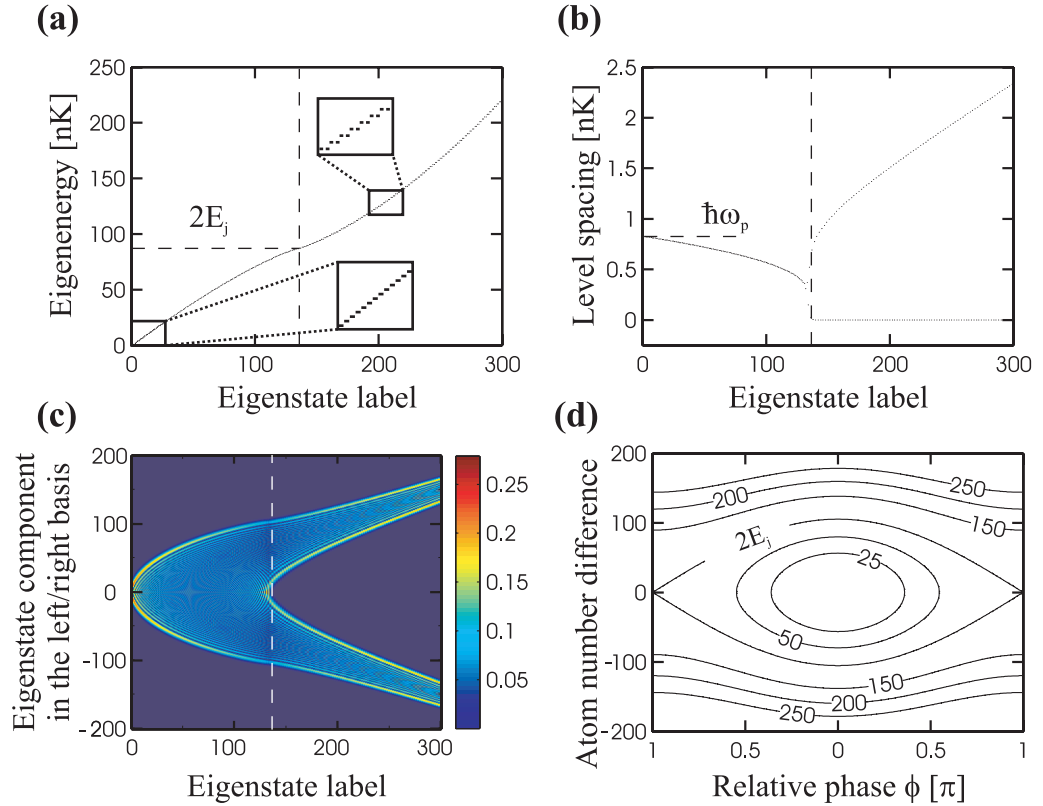


Figure 1. Lower energy eigenvalues and eigenstates of the two mode Hamiltonian in the Josephson regime ($E_C = 0.016$ nK, $E_J = 43$ nK and 3000 atoms): (a) eigenenergies, (b) eigenenergy differences, (c) eigenstates components in the left–right Fock state basis $|N/2 - n$: left, $N/2 + n$: right), (d) Phase portrait of the classical pendulum associated with the two mode model for different total energies. At low energy ($E < 2E_J$), the linear part of the spectrum corresponds to an oscillatory motion in the pendulum picture and the associated eigenstates are delocalized in the left–right basis. At higher energy, each level is two times degenerate, which corresponds to the two possible rotation directions of the pendulum twirling motion.

2.2. Calculation of the coherence factor

As we will show now, our measurement of the phase fluctuations is a direct measurement of the coherence of the system. The coherence of a many body system can be quantitatively measured by considering the first order spatial coherence function $g^{(1)}(\mathbf{r}, \mathbf{r}')$. In the two mode approximation, it is easy to see from (equation (3)) that the first order spatial coherence function does not depend on the difference $(\mathbf{r} - \mathbf{r}')$ and is constant [19]. We can then unambiguously define the coherence of the system α as the uniform value of the spatial coherence function.

$$\alpha = g^{(1)}(\mathbf{r}, \mathbf{r}') = \frac{\langle \hat{\Psi}^\dagger(\mathbf{r}') \hat{\Psi}(\mathbf{r}) \rangle}{\sqrt{\langle \hat{\Psi}^\dagger(\mathbf{r}) \hat{\Psi}(\mathbf{r}) \rangle \langle \hat{\Psi}^\dagger(\mathbf{r}') \hat{\Psi}(\mathbf{r}') \rangle}} = \frac{\langle \hat{c}_1^\dagger \hat{c}_r + \hat{c}_r^\dagger \hat{c}_1 \rangle}{N} = \frac{\langle \hat{c}_s^\dagger \hat{c}_s - \hat{c}_a^\dagger \hat{c}_a \rangle}{N}. \quad (12)$$

In the two mode approximation, the coherence of the system is simply given by the relative population difference between the symmetric and the antisymmetric state.

A more descriptive measure for phase fluctuations is the mean fringe visibility. The visibility of a single interference pattern is always high and only reduced by an initial population imbalance between the wells and the resolution of the detection method, but it is independent on temperature [20]. However, the mean fringe visibility is the visibility of ensemble averaged interference patterns and if the phase fluctuates from measurement to measurement the averaging leads to a reduction of the signal corresponding to a lower visibility. The equivalence between the coherence factor defined above and the mean fringe visibility can be established in the following way. In the two mode approximation, the Fourier component of the field operator is $\hat{\Psi}(\mathbf{k}) = \hat{c}_s \phi_s(\mathbf{k}) + \hat{c}_a \phi_a(\mathbf{k})$. The Fourier transform of the symmetric and the antisymmetric state correspond to fringe patterns with respectively a zero (bright central fringe) and a π phase (dark central fringe) modulated by an envelope $f(\mathbf{k})$. The ensemble averaged mean atom velocity distribution can thus be written as

$$\begin{aligned} n(\mathbf{k}) &= \langle \hat{\Psi}^\dagger(\mathbf{k}) \hat{\Psi}(\mathbf{k}) \rangle = n_s |\phi_s(\mathbf{k})|^2 + n_a |\phi_a(\mathbf{k})|^2 = \left[1 + \frac{n_s - n_a}{N} \cos(k_x d) \right] f(\mathbf{k}) \\ &= [1 + \alpha \cos(k_x d)] f(\mathbf{k}), \end{aligned} \quad (13)$$

where α is the visibility of the interference patterns. Assuming that the interactions do not significantly modify the velocity distribution of the atoms after a time of flight, equation (13) shows that the mean visibility factor is equal to the relative population difference between the symmetric and antisymmetric states and thus to the coherence factor α (equation (12)).

2.3. Finite temperature

At finite temperature the coherence of the BJJ is determined by quantum mechanical but also thermally induced fluctuations. To model thermal effects, we consider the two mode approximation for the condensed fraction and treat the particles in higher lying excited states as a thermal bath. We neglect the influence of the thermal distribution on the ground and the first excited states and thus on the parameters E_C and E_J . This assumption is justified if the density of the thermal cloud is low compared to the total peak density.

This allows us to calculate the density matrix using the calculated eigenenergy spectrum and thus any thermally averaged quantity. In the following, we compare the numerically obtained coherence factor with analytic predictions for the low and the high temperature limit.

2.3.1. Low temperature limit. We define the low temperature regime as the range corresponding to temperatures on the order of the plasma frequency up to the Josephson energy. In this regime, both quantum and thermal fluctuations play a role, but their overall contribution is small enough so that the coherence factor is close to 1. Following a Bogoliubov approach, we can calculate analytically the expression of the coherence factor. As shown in [21], starting from the two mode Hamiltonian, the Bogoliubov transformation is straight forward since only one quasiparticle mode can exist. The transformed Bogoliubov Hamiltonian writes

$$\hat{H}_{\text{Bg}} = E_{\text{Bg}}(N) + \hbar \omega_p (\hat{g}^\dagger \hat{g} + 1/2). \quad (14)$$

$E_{\text{Bg}}(N)$ is a constant energy term. The excitation creation operator is $\hat{g}^\dagger = u\hat{c}_a^\dagger + v\hat{c}_a$ where $u = \cosh \chi$, $v = \sinh \chi$ and $\tanh 2\chi = E_C/(E_C + 8E_J/N^2)$ [21]. The obtained excitation spectrum corresponds to the linear part of the exact spectrum plotted in figure 1(a).

To determine the coherence factor, we calculate the number of atoms in the antisymmetric state by

$$n_a = \langle \hat{c}_a^\dagger \hat{c}_a \rangle = \langle \hat{g}^\dagger \hat{g} \rangle (u^2 + v^2) + v^2. \quad (15)$$

We find the usual formula for the condensate depletion: the first term corresponds to thermal fluctuations and the second term to quantum depletion. The coherence factor is then

$$\langle \alpha \rangle = 1 - 2\frac{n_a}{N} \simeq 1 - \frac{1}{2} \sqrt{\frac{E_C}{E_J}} \left(\frac{1}{\exp(\beta\hbar\omega_p) - 1} + \frac{1}{2} \right). \quad (16)$$

with $\beta = (k_B T)^{-1}$. In the last equality, we have used the assumption that we are in the Josephson regime ($E_J/N^2 \ll E_C$). The decoherence due to quantum fluctuations is proportional to $\sqrt{E_C/E_J}$ and is always small in the Josephson regime. In figure 2, we compare this analytical result with an exact numerical calculation of α for different temperatures. We observe that the Bogoliubov result is only verified when the condensate depletion is sufficiently small which corresponds to temperatures below the Josephson energy.

2.3.2. High temperature limit. For temperatures much higher than the mean level spacing, which is approximately given at low energy by the plasma energy, a semi-classical calculation of the thermal average fringe visibility is valid. The two mode Hamiltonian corresponds to the following classical Hamiltonian [22]

$$H_{\text{Cl}} = E_C \frac{n^2}{2} - E_J \sqrt{1 - \frac{4n^2}{N^2}} \cos \phi, \quad (17)$$

where n is half the atom number difference between the two wells and ϕ is the relative phase between the two wells.

In this picture, the coherence factor corresponds to the mean value of $\cos \phi$ which writes

$$\langle \cos \phi \rangle = \frac{1}{Z} \int \cos \phi \exp(-\beta H_{\text{Cl}}) \quad \text{where } Z = \int \exp(-\beta H_{\text{Cl}}). \quad (18)$$

In the Josephson regime, the relatively strong interaction term prevents any contribution of large values of n in the previous integral. The coherence factor can then be approximated by ([10])

$$\alpha = \langle \cos \phi \rangle = \frac{\int \cos \phi \exp(-\beta E_J \cos \phi)}{\int \exp(-\beta E_J \cos \phi)} = \frac{I_1(\beta E_J)}{I_0(\beta E_J)}, \quad (19)$$

where $I_i(j)$ are the modified Bessel functions of the first kind. Figure 2 shows the comparison of this analytical expression with the exact numerical calculation for different temperatures and two different Josephson energies. At high temperature, the agreement is always very good. At low temperature and if the Josephson energy is smaller than approximately $10E_C$, a small discrepancy can appear because of quantum fluctuations (see right-hand side graph in figure 2). To use the

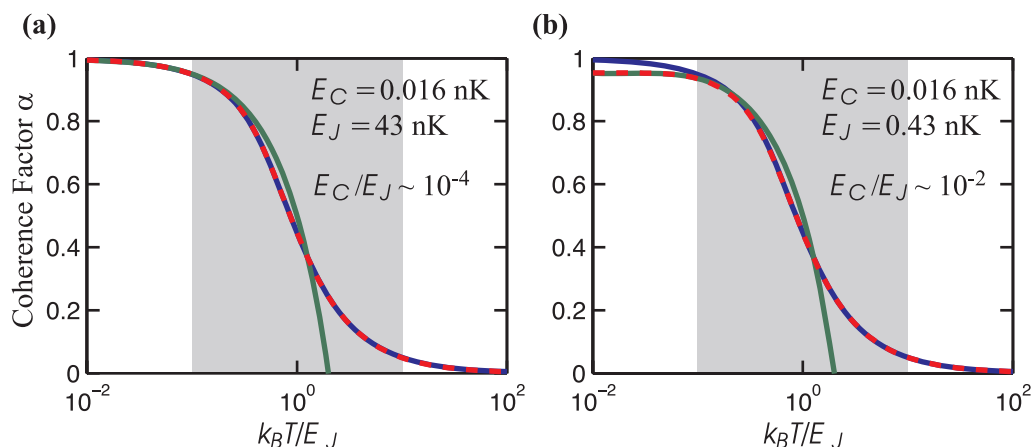


Figure 2. Coherence factor α as a function of the ratio $k_B T/E_J$ for 3000 atoms. The dashed red curve shows the result of the exact numerical calculation. The green curve is the Bogoliubov calculation (16) which is valid only at low temperature and correctly accounts for quantum fluctuations (right-hand side graph). The blue curve is the result of the semi-classical calculation (19) which is valid at high temperature and also at low temperature if quantum fluctuations are negligible (left-hand side graph). The grey shaded area corresponds to the region where the measurement of the coherence factor can be used for thermometry.

coherence factor measurement for thermometry, we always place ourselves in the situation shown in the left-hand sidegraph of figure 2 where the agreement between the exact calculation and the semi-classical formula (equation (19)) is better than 1%. In this case, the coherence factor only depends on the dimensionless parameter βE_J , the conversion between the two quantities being precisely given by equation (19). Since the phase fluctuations depend strongly on the temperature in the range of $0.1E_J$ and $10E_J$ (see grey shaded area in figure 2), this regime is ideally suited for deducing the temperature from phase fluctuation measurements. This dynamic range can furthermore be tuned by adjusting the coupling strength E_J . Once the parameter βE_J is known from the coherence measurement, the conversion to a temperature relies on a precise calculation of E_J . The main uncertainty in this calculation comes from the atom number uncertainty.

3. Experimental protocol

In this section, we give an overview of our experimental thermometry procedure. Our experimental setup has already been described in detail in [23]. The experiment is performed as follows. We first generate a single BEC by loading a precooled ^{87}Rb sample in a 3D optical dipole trap as indicated in figure 3(a). The harmonic trapping frequencies are $\omega_x = 2\pi \cdot 90(2)$ Hz and $\omega_{y,z} = 2\pi \cdot 100(2)$ Hz. Evaporative cooling is performed until the number of particles in the trap is lowered usually to about 2000–4000 and the lowest accessible temperature $T = 15(4)$ nK is reached. Holding the atoms in the trap for a given time allows for increasing the temperature of the sample in a controlled way. The heating rate in the optical trap is about 2 nK s^{-1} for a classical gas (see section 6). Once the final temperature is reached, the harmonic potential is transformed into the double-well potential by slowly ramping up a standing light wave of the

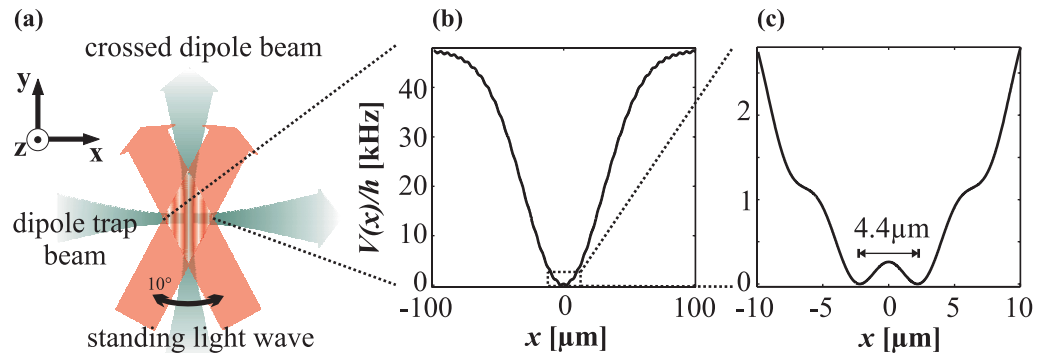


Figure 3. Experimental setup and realization of the double-well potential by the superposition of a harmonic trap and an optical lattice with large periodicity. Panel (a) is a sketch of the laser beams generating the optical potentials. Two orthogonal dipole trap beams at 1064 nm (grey) create a 3D harmonic confinement and two laser beams at 830 nm crossing under an angle of 10° generate the optical lattice (red) with a periodicity of $\lambda = 4.8 \mu\text{m}$. Panel (b) shows the effective potential resulting from the superposition of the dipole trap and the optical lattice on the scale of the Gaussian dipole trap beam. Panel (c) is the potential in the centre of the trap revealing the effective double-well trap with a separation of the two wells of $4.4 \mu\text{m}$.

form $V = V_0/2 \cdot (1 + \cos(2\pi \cdot x/\lambda))$ with $\lambda = 4.8(2) \mu\text{m}$. The resulting potential is shown in figures 3(b) and (c). The optical lattice is generated by two interfering laser beams (830 nm) crossing under an angle of 10° . The angle is chosen such that the distance between the two wells is larger than the optical resolution of $3.2(2) \mu\text{m}$ (sparrow-criterion). The barrier is ramped up in 300 ms in order to prevent excitation of the condensates in each well and to guarantee thermal equilibrium. The coupling strength due to tunnelling between the two wells can be adjusted by changing the barrier height. Typically, we vary V_0/h between 500 and 2500 Hz (the chemical potential ranges between 600 and 900 Hz). Under these conditions, the distance between the two wells is approximately $4.4 \mu\text{m}$ as shown in figure 3(c).

The relative phase between the two condensates is measured after a time of flight of 5 or 6 ms. Typical interference patterns are shown in figures 4(b) and (c). Figure 4(b) corresponds to measurements at low temperature ($T = 15(4) \text{ nK}$) and (c) to high temperature ($T = 80(2) \text{ nK}$). The single images show a clear interference signal with high visibility (usually larger than 50%). In order to fit the relative phase, the images are integrated transversally to the interference patterns (central graphs). At high temperature a broad incoherent background becomes visible resulting from the ballistic expansion of the thermal atoms. To fit the interference patterns at high temperature, this background is subtracted. The resulting profiles (lower graphs) thus correspond only to the coherent part of the matter wave interference. The fitting procedure leads to an uncertainty of the relative phase of about 0.13π .

Repeating the interference experiments reveals that the relative phase is not constant but fluctuates around zero as shown in figure 5. The fluctuations increase with increasing temperature and decrease with increasing tunnelling coupling. This shows qualitatively that two competing processes are relevant for the thermally induced fluctuations of the relative phase, namely thermal effects leading to a randomization of the phase and the coherent tunnelling coupling to a stabilization of the phase.

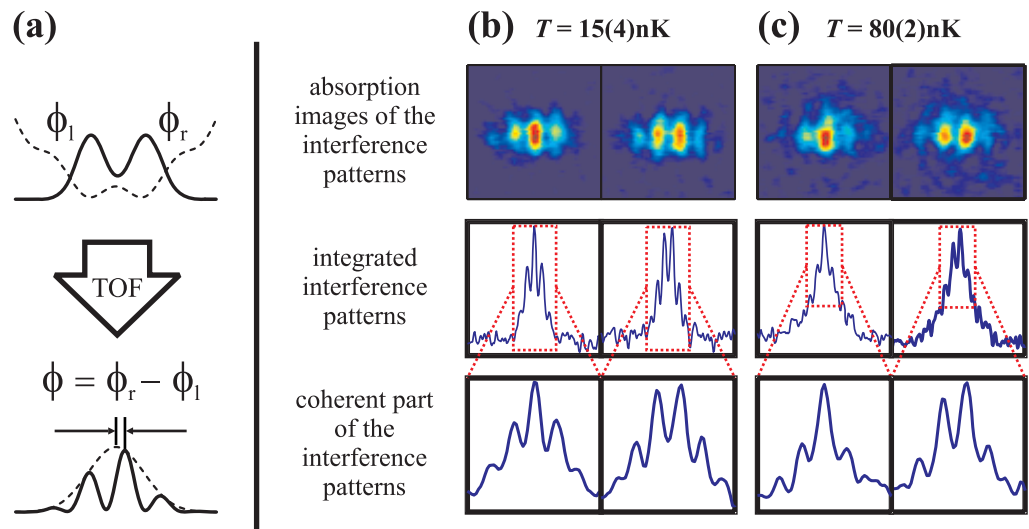


Figure 4. Matter-wave interference patterns. Panel (a) is a sketch of the interference experiments. Once the double-well trap is turned off, the matter-wave packets expand, overlap and interfere. Panel (b) corresponds to typical interference patterns for low temperature and panel (c) to typical interference patterns for high temperature. The integrated patterns show a clear interference signal for all temperatures (central graphs). However, for high temperature also a broad background is visible, corresponding to the distribution of the thermal atoms after the expansion time. In order to find the coherent interference patterns, this background is subtracted (lower graphs).

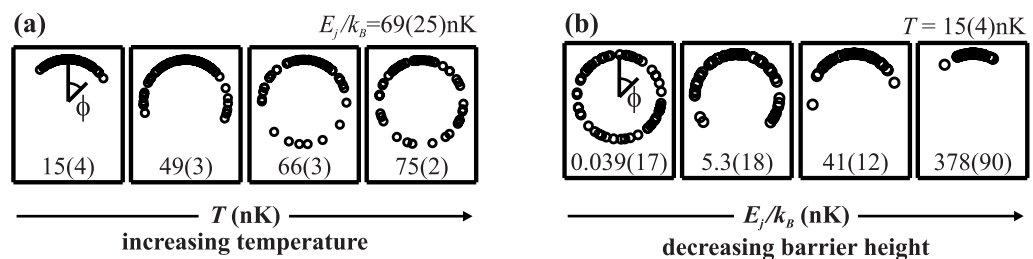


Figure 5. Qualitative behaviour of the fluctuations of the relative phase. The black circles correspond to single measurements of interference patterns in a polar plot. Panel (a) shows the change of the fluctuations as a function of temperature where the coupling strength is kept constant. With increasing temperature the fluctuations increase. Panel (b) shows the behaviour of the fluctuations for decreasing barrier heights leading to an increase of the coupling strength. The temperature is kept constant. Due to the increase of the coupling, the fluctuations are decreased demonstrating the stabilizing effect of the tunnelling coupling.

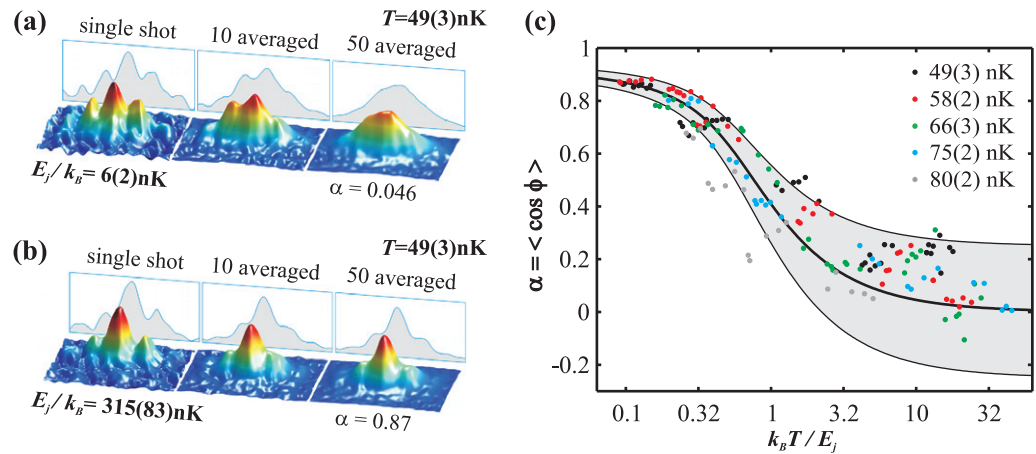


Figure 6. Experimental investigation of the coherence factor α . Panel (a) shows the transition from coherent single realizations to incoherent ensemble averages. The first picture shows that for single realizations a clear interference picture is observed. For small tunnelling coupling ($E_J = 6(2)$ nK) compared to the thermal energy ($T = 49$ nK), the averaging over many images leads to the loss of the visibility which is directly connected to the loss of the coherence ($\alpha = 0.046$). Panel (b) visualizes that for large coupling ($E_J = 315(83)$ nK) the averaging over many realizations does not destroy the coherence ($\alpha = 0.87$) and leads only to a small degradation of the visibility. Panel (c) shows the quantitative behaviour of the coherence factor α as a function of the scaling parameter $k_B T/E_J$. Each data point corresponds to the averaging over at least 28 (in average 40) single measurements for different T and E_J . The temperature is measured independently with time of flight measurements and the coupling strength is deduced from 3D simulations of the BJJ using independently measured system parameters (potential parameters and atom numbers). The experimental error of $k_B T/E_J$ is about $\pm 30\%$. The central black line corresponds to the prediction of the classical theory and also takes the uncertainty of the phase-fitting into account. The grey shaded area shows twice the expected standard deviation of the coherence factor due to the finite number of measurements. The behaviour of the coherence factor is confirmed over a three orders of magnitude change of the scaling parameter.

4. Coherence factor—scaling law for phase fluctuations

The coherence factor α (equation (19)) is in the thermodynamic limit a measure for the fluctuations of the relative phase [11] and is directly connected to the visibility of the ensemble averaged interference patterns as discussed in subsection 2.2. It predicts the coherence factor of the BJJ if quantum mechanical fluctuations are negligible ($\hbar\omega_p \ll k_B T$) and thus corresponds to an upper bound for the measurements. For large $k_B T/E_J$, the phase fluctuates strongly from shot to shot and causes a reduction of the ensemble averaged visibility. This corresponds to a small coherence factor as visualized in figure 6(a). By increasing the tunnelling coupling the coherence of the system can be regained as shown in figure 6(b).

The quantitative measurement of the coherence factor α as a function of the scaling parameter $k_B T/E_J$ is shown in figure 6(c). For this, we performed up to 100 measurements with a condensate

fraction ranging between 1000 and 4000 atoms at different temperature and different barrier heights (which means that at high temperatures the total number of atoms is approximately 10000). In figure 6(c), every data point corresponds to a subset extracted from these measurements for different atom number ranges (e.g. 2000–2500, 2500–3000 etc. atoms in the condensate fraction). The Josephson energy E_J is then calculated for every point at the given trap parameters and the mean atom numbers in the BEC by numerically solving the Gross–Pitaevskii equation in 3D. The influence of the thermal atoms is neglected. Each data point represents at least 28 single measurements and on average 40 measurements. The coherence factor is calculated by averaging over the cosine of the fitted phases.

The temperature corresponding to the data points is measured with three different methods. In the single interference images, it is possible to fit the thermal background transversally to the interference patterns. The temperature is then connected to the waist of the thermal cloud and to the time of flight. Additionally, independent time of flight measurements are performed releasing the atoms from the harmonic trap and the temperature deduced from both the expansion velocity of the thermal cloud and the ratio between condensate and thermal fraction. All three methods lead within the experimental error to the same results. The temperatures used for $k_B T/E_J$ in figure 6(c) are extracted from the time of flight measurements using the last method.

The typical error of $k_B T/E_J$ is $\pm 30\%$. The error in E_J results from the uncertainty of the atom numbers, the trapping frequencies, the barrier height and the lattice spacing of the periodic potential. The error in T results from the fitting error of the waists and amplitudes of the double gaussian distribution of the independent time of flight measurements.

The central black line in figure 6(c) shows the theoretical prediction for the coherence factor taking the fitting error of the relative phases into account. The influence of the fitting error on the coherence factor can be estimated by introducing an additional fluctuating phase and averaging over it. The distribution of the additional phase is approximated by a box function with a standard deviation corresponding to the fitting error. The averaging leads to a reduction of the coherence factor

$$\begin{aligned} \alpha' = \langle \cos(\phi) \rangle' &= \frac{\int_{-\phi_0}^{\phi_0} d\phi' \int_{-\pi}^{\pi} d\phi \cos(\phi - \phi') \exp(E_J/k_B T \cos(\phi))}{\int_{-\phi_0}^{\phi_0} d\phi' \int_{-\pi}^{\pi} d\phi \exp(E_J/k_B T \cos(\phi))} \\ &= \frac{\sin(\phi_0)}{\phi_0} \frac{\int_{-\pi}^{\pi} d\phi \cos(\phi) \exp(E_J/k_B T \cos(\phi))}{\int_{-\pi}^{\pi} d\phi \exp(E_J/k_B T \cos(\phi))} = \frac{\sin(\phi_0)}{\phi_0} \alpha. \end{aligned} \quad (20)$$

For our experiments ϕ_0 is equal to 0.23π which corresponds to a fitting error of $\sqrt{\frac{1}{2\phi_0} \int_{-\phi_0}^{\phi_0} \phi^2 d\phi} = 0.13\pi$ of the relative phase and to a reduction of the coherence factor $\alpha' = 0.92\alpha$. The grey shaded area shows twice the standard deviation of the coherence factor resulting from the finite number of measurements. For about 40 measurements, it can be estimated by $\Delta\alpha \approx (1 - \alpha)/8$.

The observed behaviour of the coherence factor is consistent with the two mode model prediction over three orders of magnitude of the scaling parameter $k_B T/E_J$. For small values of $k_B T/E_J$, the coherence factor is in close agreement with the theoretical prediction. However, for $k_B T/E_J > 2$ the data points lie within the experimental error but are mainly localized above the curve. This deviation can be explained by the fact that the BJJ is not thermalized for small E_J (see section 6). The points corresponding to high temperature lie outside the shaded region showing a lower degree of coherence. A disagreement in this regime can also be expected as

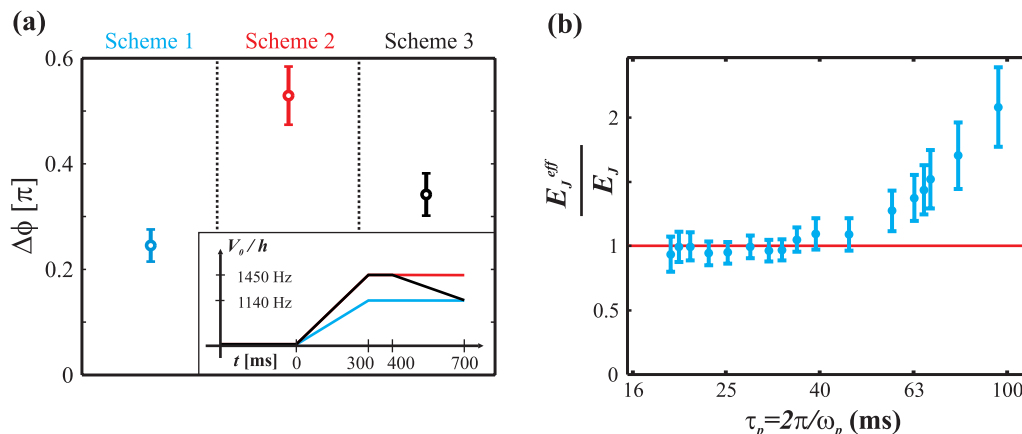


Figure 7. Experimental test for thermal equilibration of the BJJ. In panel (a), three different ramps as indicated are compared. The decrease of the fluctuations for scheme 3 with respect to scheme 2 indicates the thermalization process and the stabilizing effect of the tunnelling coupling. Panel (b) shows the comparison of the measured coherence factors and the theoretical expectation. The experimental E_J^{eff} are deduced by fitting the measured coherence factor to the theoretical prediction. For tunnelling times $\tau_p \leq 50$ ms the ratio is 1 and no correction is needed. For $\tau_p > 50$ ms the ratio increases as the BJJ is not completely thermalized. Thermalization takes only place if $\tau_p \ll t_{\text{ramp}} = 300$ ms, which is the time for ramping up the potential barrier.

the temperature of 80 nK is close to the critical temperature of $T_c \approx 87$ nK. In this regime, the excitation spectrum may not be correctly accounted for by the two mode model.

5. Thermalization

The theoretical prediction for the coherence factor is only valid in thermal equilibrium. In order to check for thermal equilibration, different experimental tests have been performed.

We have compared the fluctuations of the relative phase after three different ramping schemes as shown in figure 7(a). For these measurements, the atom number is 4000(400). In scheme 1, the barrier is ramped up to a low value ($V_0 = 1140$ Hz) within 300 ms and then kept the barrier constant for 400 ms. Scheme 2 is similar to scheme 1 but with a higher final value of the barrier ($V_0 = 1450$ Hz). As expected, the fluctuations are small for scheme 1 and larger for scheme 2. Scheme 3 is a combination of the two previous schemes. Initially the barrier is ramped up to the higher value ($V_0 = 1450$ Hz) within 300 ms, then the barrier is kept constant for 100 ms and then the barrier is ramped down to the lower value ($V_0 = 1140$ Hz) within 300 ms. The fluctuations measured according to scheme 3 are smaller than those measured according to scheme 2, indicating a thermalization process. This leads to the counterintuitive behaviour that phase fluctuations can be decreased by thermalization processes.

To get a more quantitative handle on thermalization, we compare the coherence factor measurements with the theoretical prediction from equation (19). We introduce an effective tunnelling coupling E_J^{eff} to account for out of equilibrium situations and deduce $k_B T / E_J^{\text{eff}}$ from

the experimental data shown in figure 6. In figure 7(b), the ratio E_J^{eff}/E_J is shown as a function of the tunnelling time $\tau_p = 2\pi/\omega_p \propto 1/\sqrt{E_J}$. We find that for the chosen ramping time of 300 ms, the effective tunnelling coupling is only equal to the numerically calculated tunnelling coupling for $\tau_p < 50$ ms. Thus for the application as a primary thermometer, care has to be taken to choose the appropriate tunnelling parameters. The observed increase of E_J^{eff} for large tunnelling times ($\tau_p > 50$ ms which corresponds to $E_J < 60$ nK), could be explained by the fact that the system may still have not reached equilibrium after the 300 ms ramp.

6. Application of the thermometer to heat capacity measurement

From the previous discussion, it follows that if the tunnelling rate is sufficient to guarantee thermal equilibrium ($\tau_p < 50$ ms for a 300 ms ramping up time of the potential barrier), the measurement of the phase fluctuations and an independent determination of the coupling strength E_J constitute a primary thermometer.

To test the applicability of the new thermometer, we measure the heating up of a degenerate Bose gas in a 3D harmonic trap. For this, the BEC is prepared at the lowest accessible temperature and the cooling is turned off. The phase fluctuations are then measured after different holding times by ramping up the barrier within 300 ms to barrier heights corresponding to a coupling strength on the order of the thermal energy scale. About 60 interference patterns are produced for every holding time in the harmonic trap. For longer holding times, where the thermal fraction becomes visible, also time of flight measurements from the 3D harmonic trap are performed. The results are shown in figure 8. The blue points correspond to temperature measurements using the phase fluctuation method and the open circles to measurements using the standard time of flight method. We observe the heating after a holding time of up to 36 s. After 25 s the critical temperature of $T_c = 59.1$ nK is reached and the condensate fraction vanishes. For these measurements the total number of atoms in the trap is kept constant, thus the phase fluctuation measurements can only be performed up to 6 s as long as the condensate fraction is large enough to observe clear interference patterns. Below 30 nK, the time of flight method cannot be applied as the fraction of thermal atoms in this regime is too small and cannot be fitted.

The increase of the temperature with time can be explained by taking the dependence of the heat capacity on temperature of a Bose gas into account and assuming a constant transfer of energy. For short holding times a fast increase of the temperature corresponding to a large heating rate can be observed. The heating rate decreases continuously until the critical temperature is reached, above the critical temperature the heating rate stays constant. We attribute this decrease of the heating rate to an increase in the specific heat as expected for a degenerate Bose gas. We assume the specific heat to be proportional to $(T/T_c)^d$ below T_c and constant afterwards [24]. The expected evolution of the temperature with time t is then

$$T(t) = \begin{cases} \sqrt[d+1]{h_0 T_c^d t + T(0)^{d+1}} & \text{for } T_{\text{fit}} < T_c \\ h_0 t + T(0) & \text{for } T_{\text{fit}} \geq T_c, \end{cases} \quad (21)$$

where h_0 is the constant energy transfer rate and the critical temperature is deduced from independent measurements of the trap parameters and atom numbers $T_c \approx 0.94 \cdot \hbar/k_B \cdot (\omega_x \omega_y \omega_z)^{1/3} \cdot N^{1/3} = 59.1$ nK. Using this function to fit the observed temperature increase, we obtain $h_0 = 2.4(1)$ nK and a dimensionality parameter $d = 2.4(4)$.

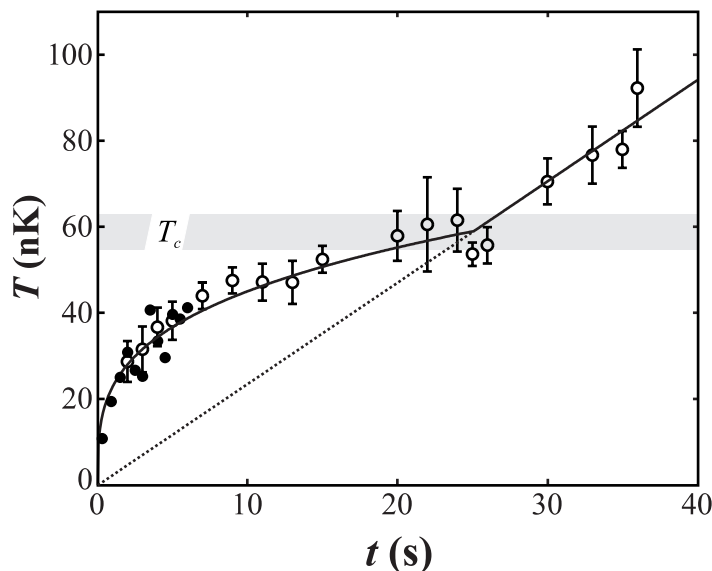


Figure 8. Thermometry using phase fluctuations measurements. The graph shows the application of the phase thermometer. The temperature of a degenerate Bose gas is plotted as a function of the holding time in the harmonic trap. The blue points correspond to measurements using the phase fluctuation method (for the few points where $\tau_p > 50$ ms, we slightly correct the calculated temperatures using the effective Josephson energy plotted in figure 7(b)) and the ‘o’ to measurements applying the standard time of flight method. In the overlap region both methods lead to the same results showing the applicability of the noise thermometer. The black line corresponds to a fitting function assuming a constant transfer rate of energy, a power law for the temperature-dependent heat capacity below the critical temperature and a constant heat capacity above. The measurements demonstrate the deviation of the heat capacity of the Bose gas from the classical gas.

The most likely source of heating in these experiments are fluctuations of the trap position and the trapping frequencies. The heating due to fluctuations of the trap position corresponds to a constant increase of energy per time and particle and the heating due to fluctuations of the trapping frequencies (parametric heating) to an exponential increase of the energy [25]. The fitting with a function taking both heating processes into account reveals that the additional increase due to parametric heating is very small and results in a correction of the temperature of below 7% after the 36 s with $d = 2.7(7)$. Thus, the assumption of a constant transfer rate of energy describes the experimental situation very well.

The observation of the heating for low temperatures represent the extension of the heat capacity measurements already performed in the early days of BEC [26] to the low temperature limit. The data clearly revealed that the heat capacity of a degenerate interacting Bose gas is smaller than the classical gas prediction for temperatures below $0.7 \times T_c$. The dimensionality deduced from our data is slightly smaller than the theoretical prediction $d = 3$ for the heat capacity of an ideal Bose gas confined in a 3D harmonic trap, as expected due to the presence of atom–atom interaction [27]. Clearly the dependence of the heat capacity on the temperature with $d > 1$ confirms the prediction of the third law of thermodynamics [28] stating that the heat capacity has to vanish in the zero temperature limit.

From this analysis, we can conclude that the phase fluctuation measurements can be applied for thermometry without the need for calibrating the thermometer with independent methods. However, a more detailed understanding on the thermalization process and the relevant timescale is necessary to be able to predict the range of validity for the measurements.

7. Conclusion

In summary, we have presented a detailed analysis of a new method for measuring ultralow temperatures of degenerate Bose gases in a regime where standard time of flight methods cannot be applied. These temperature measurements were done by investigating thermally induced fluctuations of the relative phase between two weakly coupled BECs. We have compared the experimentally obtained coherence factor with the theoretical prediction using a standard two mode model at finite temperature. We found quantitative agreement over a wide range of the relevant scaling parameter. With this a primary thermometer is realized. However, it is important to note that due to the approximations in the theoretical model, this method leads to good results for low temperatures (far below the critical temperature) and if quantum mechanical fluctuations are negligible. Furthermore, care has to be taken for the preparation of the BJJ such that thermal equilibrium is guaranteed, i.e. the ramping of the barrier has to be much slower than the tunnelling time.

The application of this noise thermometer was demonstrated by measuring the heating up of a quantum degenerate Bose gas. The observed temperature increase reveals in a direct way that the heat capacity of the Bose gas below the critical temperature deviates strongly from the heat capacity of a classical gas and vanishes in the zero temperature limit as predicted by the third law of thermodynamics.

Acknowledgments

We thank T Bergeman very much for the numerical calculation of the relevant parameters and the valuable theoretical support. We also thank A Trombettoni for discussions, M Albiez and J Foelling for their contributions to the experiments, M Scherer for implementing the 3D Gross–Pitaevskii code, and D Weiskat for his indispensable help with the electronics. This work was funded by Deutsche Forschungsgemeinschaft Schwerpunktsprogramm SPP1116 and by Landesstiftung Baden–Württemberg–Atomoptik. RG thanks the Landesgraduiertenförderung Baden–Württemberg for the financial support.

References

- [1] Schumm T, Hofferberth S, Andersson L M, Wildermuth S, Groth S, Bar-Joseph I, Schmiedmayer J and Krueger P 2005 Matter-wave interferometry in a double well on an atom chip *Nat. Phys.* **1** 57–62
- [2] Saba M, Pasquini T A, Sanner C, Shin Y, Ketterle W and Pritchard D E 2005 Light scattering to determine the relative phase of two Bose–Einstein condensates *Science* **307** 1945
- [3] Albiez M, Gati R, Foelling J, Hunsmann S, Cristiani M and Oberthaler M K 2005 Direct observation of tunneling and nonlinear self-trapping in a single bosonic Josephson junction *Phys. Rev. Lett.* **95** 010402
- [4] Likharev K K 1979 Superconducting weak links *Rev. Mod. Phys.* **51** 101–69
- [5] Barone A and Paterno G 1982 *Physics and Applications of the Josephson Effect* (New York: Wiley)

- [6] Davis J C and Packard R E 2002 Superfluid ^3He Josephson weak links *Rev. Mod. Phys.* **74** 741–73
- [7] Sols F 1994 Randomization of the phase after suppression of the Josephson coupling *Physica B* **194–6** 1389–90
- [8] Imamoglu A, Lewenstein M and You L 1997 Inhibition of coherence in trapped Bose–Einstein condensates *Phys. Rev. Lett.* **78** 2511–4
- [9] Leggett A J 2001 Bose–Einstein condensation in the alkali gases: some fundamental concepts *Rev. Mod. Phys.* **73** 307–56
- [10] Pitaevskii L and Stringari S 2001 Thermal vs quantum decoherence in double well trapped Bose–Einstein condensates *Phys. Rev. Lett.* **87** 180402
- [11] Gati R, Hemmerling B, Foelling J, Albiez M and Oberthaler M K 2006 Noise thermometry with two weakly coupled Bose–Einstein condensates *Phys. Rev. Lett.* **96** 130404
- [12] Andrews M R, Townsend C G, Miesner H-J, Durfee D S, Kurn D M and Ketterle W 1997 Observation of interference between two Bose condensates *Science* **275** 637–41
- [13] Dettmer S *et al* 2001 Observation of phase fluctuations in elongated Bose–Einstein condensates *Phys. Rev. Lett.* **87** 160406
- [14] Richard S, Gerbier F, Thywissen J H, Hugbart M, Bouyer P and Aspect A 2003 Momentum spectroscopy of 1D phase fluctuations in Bose–Einstein condensates *Phys. Rev. Lett.* **91** 010405
- [15] Ananikian D and Bergeman T 2006 Gross–Pitaevskii equation for Bose particles in a double-well potential: two-mode models and beyond *Phys. Rev. A* **73** 013604
- [16] Milburn G J, Corney J, Wright E M and Walls D F 1997 Quantum dynamics of an atomic Bose–Einstein condensate in a double well potential *Phys. Rev. A* **55** 4318–24
- [17] Anglin J R and Vardi A 2001 Dynamics of a two-mode Bose–Einstein condensate beyond mean-field theory *Phys. Rev. A* **64** 013605
- [18] Dunningham J A and Burnett K 2004 Sub-shot-noise-limited measurements with Bose–Einstein condensates *Phys. Rev. A: At. Mol. Opt. Phys.* **70** 033601
- [19] Spekkens R W and Sipe J E 1999 Spatial fragmentation of a Bose–Einstein condensate in a double-well potential *Phys. Rev. A* **59** 3868–77
- [20] Castin Y and Dalibard J 1997 Relative phase of two Bose–Einstein condensates *Phys. Rev. A* **55** 4330–7
- [21] Paraoanu G-S, Kohler S, Sols F and Leggett A J 2001 The Josephson plasmon as a Bogoliubov quasiparticle *At. Mol. Opt. Phys.* **34** 4689–96
- [22] Raghavan S, Smerzi A, Fantoni S and Shenoy S R 1999 Coherent oscillations between two weakly coupled Bose–Einstein condensates: Josephson effects, π oscillations, and macroscopic quantum self-trapping *Phys. Rev. A* **59** 620–33
- [23] Gati R, Albiez M, Foelling J, Hemmerling B and Oberthaler M K 2006 Realization of a single Josephson junction for Bose–Einstein condensates *Appl. Phys. B* **82** 207–10
- [24] De Groot S R, Hooyman G J and ten Seldam C A 1950 On the Bose–Einstein condensation *Proc. R. Soc. Lond. A* **203** 266–86
- [25] Savard T A, O’Hara K M and Thomas J E 1997 Laser-noise-induced heating in far-off resonance optical traps *Phys. Rev. A* **56** R1095–R1098
- [26] Ensher J R, Jin D S, Matthews M R, Wieman C E and Cornell E A 1996 Bose–Einstein condensation in a dilute gas: measurement of energy and ground-state occupation *Phys. Rev. Lett.* **77** 4984–7
- [27] Minguzzi A, Conti S and Tosi M P 1997 The internal energy and condensate fraction of a trapped interacting Bose gas *J. Phys.: Condens. Matter* **9** L33–L38
- [28] Feynman R P, Leighton R B and Sands M 1963 *The Feynman Lectures on Physics* vol 1 (Reading, MA: Addison-Wesley)